Applied Catalysis B: Environmental 254 (2019) 166–173

Contents lists available at ScienceDirect

Applied Catalysis B: Environmental

journal homepage: www.elsevier.com/locate/apcatb

# Nonradical activation of peroxydisulfate promoted by oxygen vacancy-laden NiO for catalytic phenol oxidative polymerization

Lindong Liu[a,*], Qian Liu[a], Ying Wang[a], Jin Huang[a], Wenju Wang[b], Lian Duan[a], Xiao Yang[a], Xiaoyong Yu[c], Xu Han[d], Nian Liu[e]

[a] Chongqing Engineering Research Center of Biomaterial Fiber and Modern Textile, College of Textiles and Garments, Southwest University, Chongqing 400715, China
[b] School of Energy and Power Engineering, Nanjing University of Science and Technology, Nanjing 210094, China
[c] MOE Key Laboratory of Pollution Processes and Environmental Criteria, College of Environmental Science and Engineering, Nankai University, Tianjin 300071, China
[d] Key Lab of Indoor Air Environment Quality Control, School of Environmental Science and Engineering, Tianjin University, Tianjin 300072, China
[e] School of Chemical and Biomolecular Engineering, Georgia Institute of Technology, Atlanta, GA 30332, USA

ARTICLE INFO

*Keywords:*
Oxygen vacancies
Nonradical activation
Oxidative polymerization
Peroxydisulfate
NiO nanoplatelets

ABSTRACT

Engineering the electronic properties of catalysts to facilitate electron transfer and activation of dynamically stable peroxydisulfate (PDS) offers a promising strategy for efficient remediation of recalcitrant organic pollutants through heterogeneous Fenton-like processes, but also presents challenges due to a lack of facile methods. Herein, we highlight a simple defect engineering strategy that greatly increases the efficiency of PDS adsorption and activation by introducing oxygen vacancies ($V_O$) into NiO to produce an electron-rich surface. Experimental studies and density functional theory (DFT) calculations confirmed that $V_O$ confined in NiO could successfully cause synergetic effects of lower adsorption energy and more exposed active sites, thus facilitating the bonding with PDS molecules and promoting the reactivity of PDS-NiO complex, giving rise to dramatic enhancement of catalytic performance with removal rate as high as 3.978 mmol(phenol) $min^{-1}$ g(NiO)$^{-1}$. Mechanistic studies further reveal that the surface-activated PDS-NiO complex mediate oxidative polymerization of phenol (a model pollutant) involved in the generation of phenoxyl radicals and subsequent coupling reactions, providing the potential to convert recalcitrant organic pollutants into value-added products. This work may pave the way toward practical fabrication of highly efficient "defect-type" Fenton-like catalysts, and the present method also provides new opportunities to achieve sustainable wastewater treatment through reuse of organic pollutants.

## 1. Introduction

The problems of water pollution and shortage resulting from rapid industrialization and civilization have driven recent intensive efforts toward sustainable treatment of wastewater [1,2]. Peroxydisulfate ($S_2O_8^{2-}$; PDS) advanced oxidation processes (PDS-AOPs) which based on Fenton chemistry, utilizing either radical-driven processes to generate highly reactive oxygen-containing radicals (e.g., $SO_4^{\cdot -}$, $HO^{\cdot}$) or direct electron transfer to induce nonradical processes, can provide alternative solutions for remediation of persistent organic pollutants (industrial dyes, pesticides, pharmaceuticals, *etc.*) in the aquatic environment using less energy [2–6]. PDS itself has low oxidative potential ($E^o$ = 2.01 V *vs.* normal hydrogen electrode [7]) without external activation, and typically forms $SO_4^{\cdot -}$ as a secondary oxidant via activation processeses. On the other hand, nonradical activation mechanisms for PDS-AOPs were also confirmed in carbon/PDS and CuO/PDS catalytic systems in which activated PDS–catalyst complex directly degraded model pollutants not relying on the generation of oxygen-containing radicals [8,9]. PDS has high aqueous solubility and moderate cost (\$0.74 $kg^{-1}$), one-half and one-third the costs of $H_2O_2$ (\$1.5 $kg^{-1}$) and peroxymonosulfate (sold as Oxone® ($KHSO_5$•1/2$KHSO_4$•1/2$K_2SO_4$), \$2.2 $kg^{-1}$) [9]. Therefore, interest in PDS activation has become widespread. PDS is a white crystalline solid with a symmetric structure and a relative stable O—O bond (140 kJ $mol^{-1}$) [7,10], making it more chemically stable than other oxidants. Among various activation approaches, the catalytic activities of transition metal oxides are limited by the low efficiency of electron transfer to PDS, which is generally considered as the rate-limiting step in PDS activation [2,4,11,12]. For this reason, rational design of a highly active catalyst with electron-donation centers that can capture PDS and activate the stable O—O bond is especially important.

Defect engineering, the engineering of intrinsic and extrinsic defects

* Corresponding author.
*E-mail address:* lindongliu@swu.edu.cn (L. Liu).

https://doi.org/10.1016/j.apcatb.2019.04.094
Received 26 December 2018; Received in revised form 28 April 2019; Accepted 29 April 2019
Available online 03 May 2019
0926-3373/ © 2019 Elsevier B.V. All rights reserved.

such as metal vacancies ($V_M$), oxygen vacancies ($V_O$) and lattice vacancies ($V_L$), is regarded as an effective strategy to chemically tailor catalytic properties [13–16]. Over the past 60 years, defects in metal oxide semiconductors have been extensively studied for diverse purposes, including nitrogen fixation [17], $CO_2$ reduction [15], water splitting [18], and organics degradation [14] in aqueous solutions. NiO is a functional material and a representative $V_L$ semiconductor with $V_L$ at the metal site ($Ni^{2+}$) [13,16]. The easily formed $Ni^{2+}$ vacancies create a charge imbalance, corresponding to the introduction of cation holes ($h^+$) that must be counteracted. To balance the loss of $Ni^{2+}$ and overall charge reduction, the oxidation state of the neighboring $Ni^{2+}$ must be increased ($Ni^{2+} + h^+ \rightarrow Ni^{3+}$), or $V_O$ must be formed [13,16,19]. Besides, the growth condition of NiO under lower oxygen concentration may result in appreciable concentrations of intrinsic $V_O$ [20]. As a result, the catalytic behavior of NiO may be tuned and optimized. The existed Ni(III) defects in NiO have been revealed to be favorable for PDS activation [21]. However, to the best of our knowledge, no studies have implemented $V_O$ engineering strategies on NiO for PDS adsorption and activation, and investigated how effective such processes can be.

To achieve sustainable wastewater treatment, emphasizing recovery of energy and resources, remediation technologies based on synergistic effects of adsorption and oxidative polymerization provide new strategies with the potential to efficiently convert recalcitrant organics into value-added products, rather than oxidation degradation to useless intermediates or $CO_2$ and $H_2O$. Previous studies have shown treatment technologies based on adsorption and catalytic oxidation exhibited exciting advances in catalytic performance because adsorption sites enrich the target pollutants through phase separation, and catalytic sites simultaneously generate reactive species to rapidly degrade the adsorbed pollutants [10,22,23]. On the other hand, electron-rich bromophenols can be oxidized into brominated polymeric products in aqueous solution involved the generation of bromophenoxyl radicals via one-electron oxidation [24]. Given that catalytic behavior can be tailored and optimized by defect engineering, defect-laden NiO may possess superior capacities in PDS adsorption, and thus exhibit novel activation processes of PDS molecules. Furthermore, elucidation of the role of defects in PDS adsorption and activation would provide further insights into the mechanisms of Fenton chemistry, and may lead to the development of other effective "defect-type" Fenton-like catalysts.

In this work, a facile defect engineering strategy is reported for the introduction of $V_O$ into NiO to create highly reactive Fenton-like catalysts for efficient oxidative polymerization of phenol via nonradical activation of PDS. The total amounts of $V_O$ can be tuned by varying the protective gas ($N_2$/air) or changing the calcination temperature. $V_O$ with abundant localized electrons are of particular interest for the enhanced adsorption of dynamically stable PDS molecules and thus facilitates the bonding with PDS molecules and promotes the reactivity of PDS-NiO complex, as determined through experimental measurements and density functional theory (DFT) calculations. Mechanistic studies further reveal that the surface-activated PDS-NiO complex mediate oxidative polymerization of phenol involved in the generation of phenoxyl radicals and subsequent coupling reactions. $V_O$-rich NiO exhibits impressive catalytic behavior, with removal rate as high as 3.978 mmol (phenol) $min^{-1}$ $g(NiO)^{-1}$ for oxidative polymerization of phenol into oligomers. Radical scavenging experiments and 5,5-dimethyl-1-pyrolin-*N*-oxide trapped electron paramagnetic resonance (EPR) further confirmed nonradical activation of PDS. Our study provides the detailed insights into "defect-type" Fenton-like catalysts for sustainable wastewater treatment to convert aquatic recalcitrant organics into value-added products using an oxidative polymerization mechanism.

## 2. Experimental section

### 2.1. Chemicals

$NiCl_2{\cdot}6H_2O$ (98%), Potassium peroxydisulfate (PDS, ≥99.0%), ethanol (95%), *tert*-butanol (TBA, ≥99.0%), 5,5-dimethyl-1-pyrolin-*N*-oxide (DMPO, 97%), potassium ferricyanide (≥99.5%), 4-Aminoantipyrine (98%) were purchased from Aladdin Co., China. $NH_4Cl$ (99.5%), phenol (≥99.0%), $NaS_2O_3{\cdot}6H_2O$ (99%), $K_2HPO_4$ (98%), $KH_2PO_4{\cdot}2H_2O$ (99.5%), $Na_2SO_4$ (99%) were obtained from Macklin Co., Ltd, China. HCl (38%), NaOH (96%), soluble starch, aqueous ammonia (28–30%), KI (≥99.0%), $BaCl_2{\cdot}2H_2O$ (99.5%) were purchased from Chongqing Chuandong Chemical Co., Ltd, China. All other chemicals were of analytical grade or better and used without further purification. All solutions were prepared with deionized (DI) water (18.2 MΩ $cm^{-1}$). Stock solutions of PDS were freshly prepared using DI water and standardized by an iodometric method [25].

### 2.2. Catalyst preparation

r-NiO and n-NiO were prepared *via* a one-step calcination of β-Ni$(OH)_2$ precursor under $N_2$ or air atmosphere, respectively. Hexagonal β-Ni$(OH)_2$ nanoplatelets were synthesized via a modified chemical precipitation method as reported [26]. In brief, 0.5 mol $NiCl_2{\cdot}6H_2O$ was dissolved in 100 mL DI water, followed by addition of aqueous ammonia (28–30%) to adjust the pH value to 9.0, and then heated to 90 °C and maintained for 0.5 h. Under continuously stirring, 220 mL NaOH solution (0.5 M) was added slowly, further maintained at 90 °C and stirred for another 2.0 h. After cooling naturally, the resulting precipitates were centrifuged and washed for three times with ethanol and DI water, and then freeze-dried and ground finely for future use. To obtain r-NiO, freeze-dried β-Ni$(OH)_2$ was calcined under an $N_2$ atmosphere at 450 °C for 5.0 h with a heating rate of 3 °C $min^{-1}$. As reference, n-NiO was synthesized with the same procedure but calcined in air. The described synthetic method was simple and can produce large quantities of catalysts.

### 2.3. Structure characterization

Crystal structure and morphology of samples were characterized with power X-ray diffractometer (D8 Advanced, Bruker, Germany) equipped with Cu Kα radiation source, scanning electron microscopy (SEM) (S4800, HITACHI, Japan) coupled with the corresponding selected-area electron diffraction (SAED) patterns and high-resolution transmission electron microscope (TEM) (JEM-2100F, JEOL, Japan). X-ray photoelectron spectroscopy (XPS) measurements were performed on XPS instrument (ESCALAB 250Xi, ThermoFisher Scientific, America) with all binding energies calibrated by the C 1s peaks (284.8 eV) of the surface adventitious carbon. The water-soluble and surface-attached total organic carbon (TOC) were carried out using an Analytik jena Muti N/C 2100 analyzer with modules for the analysis of both liquid and solid samples. Electron paramagnetic resonance (EPR) measurements were conducted with Bruker Elexsys 580 X-band pulsed EPR spectrometer at 9.432 GHz, using a 100 kHz field modulation frequency and a 1.0 G standard modulation amplitude. DMPO trapped EPR spectra were collected on the same EPR spectrometer with a center field at 3320 G and a sweep width of 140 G at room temperature. Thermogravimetric and derivate thermogravimetric analysis were conducted with a TG 290 F3 thermogravimetric analyzer performed in $N_2$ or air atmospheres. The average size of as-prepared catalysts in aqueous solution were recorded on the Mastersizer 3000 laser particle size analyzer and the Zeta potential values at different pH were obtained on the Zetasizer Nano Z zeta potentiometer to calculate the point of zero charge (PZC). Specific surface area ($S_{BET}$) was measured by $N_2$ adsorption/desorption isotherms (Autosorb-iQ2, Quantachrome, America), and was calculated via the Brunauer–Emmett–Teller (BET) method. The concentration of

leached $Ni^{2+}$ was determined on Agilent 720 inductively coupled plasma emission spectrometer (ICP). Molecular weights were measured by Gel Permeation Chromatography (GPC) at 30 °C using a Waters 1515 instrument with tetrahydrofuran (THF) as the mobile phase at a flow rate of 1.0 mL $min^{-1}$ and three linear styragel HT3, HT4 and HT5 columns. Matrix-assisted laser desorption/ionization time-of-flight (MALDI-TOF) mass spectrometric measurement was performed on a Bruker Reflex III equipped with a 337 nm $N_2$ laser in the reflector mode and 20 kV acceleration voltage. α-Cyano-4-hydroxycinnamic acid was used as matrix. Samples were prepared from THF solution by mixing matrix. The molecular weights were determined in the reflex mode.

### 2.4. Catalytic activity

The Fenton-like catalytic performance was evaluated for phenol removal with the addition of PDS at the initial solution pH of 11.0. The reaction temperature was maintained at 303 K using a water bath shaker with 150 rpm. In a typical experiment, 0.15 g catalyst was introduced into the DI water at the desired pH value to equilibrate for 1.0 h. Reactions were initiated by adding predetermined volume and pH value of phenol and PDS stock solutions into the above equilibrium solutions with/without a constituent of interest (i.e., ethanol, TBA, or $Cl^-$), with a final working volume of 150 mL containing 2.34 mM phenol and 4.0 mM PDS. At predetermined time intervals, the reaction solution was withdrawn to achieve the solid/water separation using a filter. The obtained aqueous supernatants were used to directly analyze the concentrations of phenol, PDS, $Ni^{2+}$, $SO_4^{2-}$, and the water-soluble TOC. The separated solid oxides were also collected for further characterization. In recycling experiment, the catalyst was recycled by refrigerated centrifugation and washed thoroughly with DI water after each run. Kinetic experiments were performed in the dark (without light irradiation) to avoid the possible photochemical reactions. All kinetic experiments were conducted in duplicate and the averaged data were presented.

Concentrations of phenol and $SO_4^{2-}$ were quantified by 4-aminoantipyrine and $BaCl_2$ turbidimetrical methods as reported in our previous study [27], and spectrophotometry was performed on UV/V-1200 spectrophotometer (Mapada, Shanghai, China) with the detection wavelength of 510 nm and 650 nm, respectively. PDS concentration was determined by an iodometric method [25].

### 2.5. First-principles simulations

Spin-polarized DFT calculations were carried out using the projector augmented wave (PAW) method implemented in the Vienna Ab initio Simulation Package (VASP) to describe the electron-core interaction [28]. The GGA-PBE was used for the exchange-correlation potentials [29], and the cutoff energy of 480 eV was selected to obtain accurate structure for all systems. The (3 × 3) and (2 × 2) supercells with four atomic layers were cleaved to mimic NiO (111) surface. The thickness of the surface vacuum layer was 20 Å to eliminate the influence of the two models. The atoms were relaxed fully until the force acting on each atom less than 0.02 eV/Å. On the other hand, the surface supercell, include nine minimal surface cell (3 × 3), was also considered and a *k*-mesh of 4 × 4 × 1 was adopted to simulation. Then, the $C_6H_5O^-$ and PDS were added into cubic lattice and surface model to optimize and calculate adsorption energy, as shown in Eq. (1):

$$E_{ads} = E_{molecule+slab} - E_{molecule} - E_{slab} \quad (1)$$

where $E_{ads}$, $E_{slab}$, and $E_{molecule}$ denote the total energy of slab with adsorbate, slab, and free molecule, respectively.

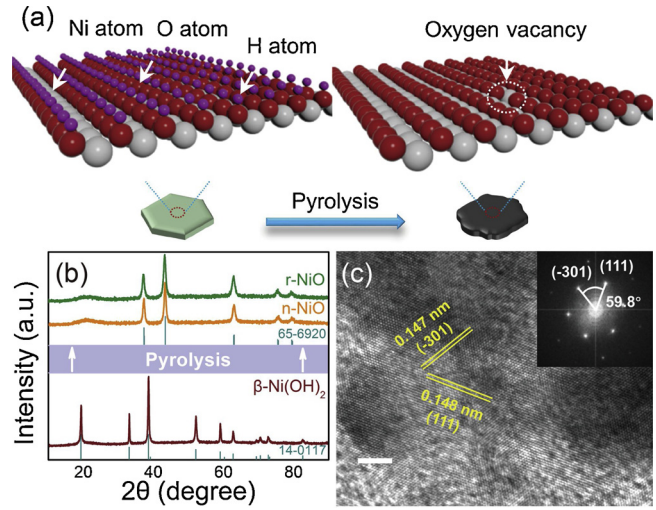


**Fig. 1.** Preparation route and structure characterization. (a) Pyrolytic synthesis of NiO catalysts. (b) Power XRD patterns of r-NiO, n-NiO and β-$Ni(OH)_2$. (c) High-resolution TEM image of r-NiO. Insert: Fast-Fourier transform (FFT) pattern. Scale bar: 2 nm.

## 3. Results and discussion

### 3.1. Synthesis and characterizations of oxygen vacancy-laden catalysts

As schematically illustrated in Fig. 1a, the synthesis of $V_O$-rich NiO (denoted as r-NiO) nanoplatelets was carried out *via* one-step pyrolysis of precursors at 450 °C for 5 h under an $N_2$ atmosphere. Precursors were formed through a chemical precipitation method and could be indexed to β-$Ni(OH)_2$ (JCPDS card no. 14-0117) (Fig. 1b). Based on thermogravimetric analysis (SI Fig. S1), the main decomposition stage that occurred in the range of 250–360 °C corresponded to thermal decomposition of β-$Ni(OH)_2$ into NiO [30], forming a black powder (SI Fig. S2). After pyrolysis, the crystal structure of β-$Ni(OH)_2$ disappeared and a monoclinic NiO phase (JCPDS card no. 65-6920, space group: C2/m [No. 12]) emerged with no other phases or impurities present (Fig. 1b). High-resolution transmission electron microscopy (TEM) images (Fig. 1c) revealed well-resolved lattice fringes at spacings of 0.148 and 0.147 nm, corresponding to the expected (111) and (−301) planes of monoclinic NiO, respectively, in good accordance with X-ray diffraction (XRD) results. The corresponding fast Fourier transform (FFT) pattern (inset in Fig. 1c) also indicated a monoclinic phase. Scanning electron microscopy (SEM) images confirmed that the annealing treatment process preserved the morphology of β-$Ni(OH)_2$, comprising disordered stacked hexagonal sheets with an average edge distance of 97.2 ± 21.4 nm and thickness of 22.1 ± 3.9 nm (SI Fig. S3a–c). In addition, r-NiO exhibited a porous morphology, with nanoscale pores on the relatively rough surface (SI Fig. S3d–f), consistent with previous reports [30,31]. For comparison, normal NiO (denoted as n-NiO) was synthesized using the same procedure as r-NiO but was calcined in air. This compound exhibited similar morphology and comparable physicochemical properties to r-NiO (Fig. 1b, SI Figs. S3 and S4, and Table S1).

To confirm the presence of $V_O$ in the prepared r-NiO and n-NiO, fine-scanned O 1s X-ray photoelectron spectroscopy (XPS) was performed. As shown in Fig. 2a, the O 1s core-level spectra could be clearly deconvoluted into two characteristic peaks of oxygen atoms. Specifically, the peaks at 529.7 and 531.7 eV could be attributed to Ni−O bonding and O atoms in the vicinity of an O vacancy, respectively [32–34]. In addition, O 1s XPS spectra demonstrated the distinct $V_O$ concentration, indicating that r-NiO formed under $N_2$ possessed more $V_O$ than n-NiO. Theoretical calculations also confirmed the intrinsic $V_O$ can be more easily formed under O-poor environmental [35].

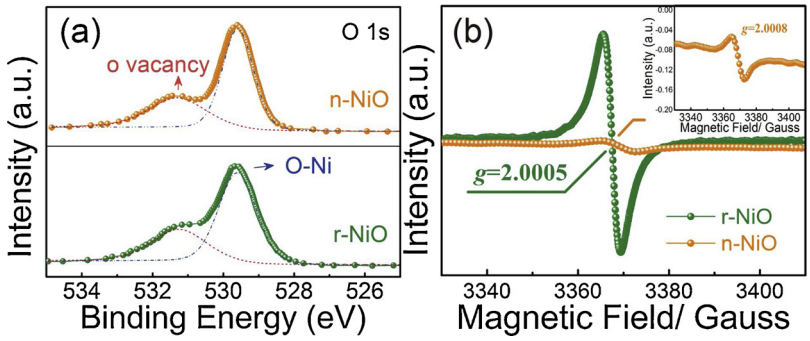


**Fig. 2.** Characterization of oxygen vacancies. (a) O 1s XPS spectra of r-NiO and n-NiO. (e) Low temperature (100 K) EPR spectra of r-NiO and n-NiO. Insert: Enlarged EPR spectrum of n-NiO.

Conversely, for $V_L$-laden NiO, more $V_O$ led to the formation of less $Ni^{3+}$ to reach charge neutrality. The Ni 2p XPS spectra (SI Fig. S5) supported this conclusion, as the binding energies of Ni $2p_{3/2}$ and $2p_{1/2}$ indicated a decreasing trend with increasing $V_O$ concentration. However, quantitative analysis of the composition ratio of $Ni^{3+}/Ni^{2+}$ was unreliable due to the complex nature of the Ni 2p spectra arising from main line broadening and multiplet splitting [36,37].

To further analyze $V_O$, EPR spectroscopy was applied to the samples. At low temperatures (100 K), the strongly symmetric EPR signal of r-NiO, with a *g*-value of 2.0005 and linewidth of 3.83 G, was identified as electrons trapped in oxygen vacancies (Fig. 2b) [14,38]. Further, the spectra fitted with a Lorentzian shape (SI Fig. S6) indicated a $V_O$ concentration of 1.12E16 $V_O\,g^{-1}$ (r-NiO). By contrast, n-NiO had a very weak $V_O$ signal at $g = 2.0008$, with a linewidth of 5.89 G (Fig. 2b) and a $V_O$ concentration estimated as 3.40E14 $V_O\,g^{-1}$ (n-NiO). The signal intensity of $V_O$ for r-NiO was markedly greater than that of n-NiO, and the $V_O$ concentration was nearly two orders of magnitude higher. Specially, at room temperature (298 K), r-NiO also exhibited an EPR signal with a *g* value of 2.0004, indicative of the presence of abundant $V_O$ (SI Fig. S7). In addition, the EPR spectrum of r-NiO showed a lower $Ni^{3+}$ signal (data not shown), implying that calcining under an $N_2$ atmosphere may result in the formation of lower quantities of $Ni^{3+}$, as also supported by Ni 2p XPS analysis (SI Fig. S5). Considering the overall characterizations and analysis using EPR and XPS, appreciable concentrations of $V_O$ are present within r-NiO compared to n-NiO; therefore, tailored and optimized Fenton-like oxidation performance is expected.

### 3.2. Catalytic performance

The Fenton-like catalytic behavior of r-NiO was evaluated in terms of phenol removal via PDS activation. All reactions were carried out at pH = 11.0 and 303 K in the dark, with the majority of phenol in its deprotonated form ($C_6H_5O^-$) due to its p*K*a value of 10.0 [39]. PDS without r-NiO was unreactive toward phenol, although base and phenol have been reported as activators of PDS (Fig. 3a) [40,41]. No adsorption of phenol onto r-NiO was also observed (SI Fig. S8). Remarkably, as much as 188.35 mg $L^{-1}$ (2.0 mM) phenol removal could be achieved in 0.5 min with 1.0 g $L^{-1}$ r-NiO and 4.0 mM PDS (Fig. 3a). Accompanying the removal of phenol, 144.21 mg $L^{-1}$ of total organic carbon (TOC) was removed from the solution within 0.5 min. In addition, two-stage reaction kinetics were observed for the coupled r-NiO/PDS process, with a rapid initial phenol decline in the first 0.5 min followed by a much slower retardation stage partly due to the limited stability of $V_O$ in the presence of PDS. The reaction rate constant (*k*) could not be calculated due to the speed of the reaction, but is expected to be significantly greater than that of n-NiO (Fig. 3a). To evaluate catalytic activity, the removal rate (mmol(phenol) $min^{-1}$ $g(NiO)^{-1}$) was calculated using the data point at 0.5 min shown in Fig. 3a [42]. Assuming that the removed TOC was completely oxidized into $H_2O$ and $CO_2$, the stoichiometric amount of PDS required was 28.05 mM (Scheme S1), which was approximately 9 times higher than the actual amount consumed. This unexpected stoichiometry of PDS/phenol precluded the oxidation degradation mechanism. In addition, the involvement of $O_2$ in air could be ruled out due to the anaerobic experimental conditions. Notably, the optimized r-NiO catalyst exhibited the most impressive catalytic performance among all reported PDS-AOPs catalysts (Table S2). Additionally, three other representative aromatic compounds (methylene blue, methyl orange, and bisphenol A) could be completely removed within 30 min at an initial solution pH of 11.0 (Table S3).

To clarify the Fenton-like catalytic processes, a series of control experiments were carried out. As shown in Fig. 3a, the precursor β-Ni$(OH)_2$ only exhibited a 7.8% phenol removal efficiency. By contrast, NiO with a $V_O$ concentration of 1.0E12 $V_O\,g^{-1}$ (denoted as p-NiO), prepared via pyrolysis of β-Ni$(OH)_2$ at 600 °C in air (physicochemical properties are shown in SI Fig. S9 and Table S1), had a phenol removal efficiency of 15.6%. The significantly enhanced catalytic properties of r-NiO suggested a crucial role of $V_O$ in catalytic PDS activation because r-, n-, and p-NiO were all purely of the monoclinic phase, with similar morphologies, comparable BET surface areas, and similar average aggregate sizes in aqueous suspensions (SI Figs. S3, S4, S9 and Table S1). Therefore, the influences of morphology, surface area, and aggregate size on Fenton-like catalytic performance could be excluded. The only difference among these catalysts was the $V_O$ concentration. In addition, the low concentration of leached $Ni^{2+}$ (0.73 mg $L^{-1}$) during reaction at an initial pH of 11.0 exhibited negligible activity in PDS activation and was below the permissible limit (1.0 mg $L^{-1}$) according to the Chinese National Standard (GB 25467-2010).

To gain further insight into the kinetics of this reaction, the influence of PDS concentration was examined. An interesting phenomenon was observed wherein the initial PDS concentration decreased from 4.0 to 0.5 mM. Within 0.5 min, 0.48 mM phenol was removed, and no further removal occurred thereafter, corresponding to the generation of 0.92 mM $SO_4^{2-}$ and consumption of 0.5 mM PDS (Fig. 3b and SI Fig. S10). The actual molar ratio of [phenol]/[PDS]/[$SO_4^{2-}$] was approximately 1:1:2. Similar effects were also observed when the initial PDS concentration was fixed at 1.0 mM, namely, when catalyst was excessive. These results indicated that the exceptional catalytic performance of r-NiO may result primarily from a one-electron oxidation mechanism with an electron donor and electron acceptor. In addition, the influence of the initial solution's pH was evaluated. Strongly basic conditions were beneficial for phenol removal compared to pH 7.12 or 9.0 (SI Fig. S11), offering a benefit over classical Fenton reagents whose oxidation capability is strictly limited by solution pH values (around pH 3.0). We also noted that overall phenol removal after 2.0 h was only slightly influenced by initial pH values within the pH range of 7.12–12.0 (SI Fig. S11), indicating that r-NiO@PDS oxidation had a wide alkaline effective pH range. From the perspective of electrostatic interactions, PDS and phenol were minimally adsorbed on the negatively charged r-NiO surface, as the $pH_{pzc}$ of r-NiO was 7.9 (SI Fig. S12). Hence, the excellent performance of the coupled r-NiO@PDS process

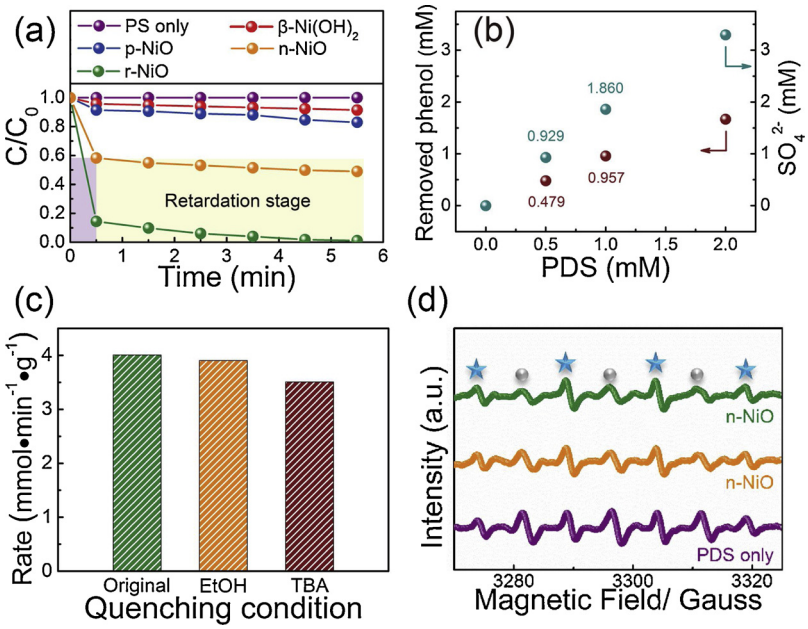


**Fig. 3.** Fenton-like catalytic performance. (a) Removal efficiency of phenol in different reaction systems catalyzed by r-NiO, n-NiO, p-NiO and β-$Ni(OH)_2$ within 5.5 min. (b) The effects of PDS dosages on phenol removal efficiency and corresponding $SO_4^{2-}$ formation from PDS activation when excessive r-NiO existed. (c) Comparison of removal rate within 0.5 min under different quenching conditions. (d) DMPO-trapped EPR spectra at 0.5 min. Reaction condition: [Phenol] = 2.34 mM, catalyst = 1.0 g $L^{-1}$, [PDS] = 4.0 mM, $T$ = 303 K, initial solution pH = 11.0, [EtOH] = 0.2 M (if needed) and [TBA] = 0.2 M (if needed).

was not dependent on electrostatic interactions. Based on the improved catalytic activity, $V_O$ engineering successfully mediated the Fenton-like catalytic activity of NiO, and $V_O$ may be the critical active sites for PDS adsorption and activation.

### 3.3. Insight into the catalytic mechanism for phenol oxidative polymerization

Indirect competitive kinetic approaches were used to evaluate the differential contributions of oxygen-containing radicals ($SO_4^{\cdot -}$ and $HO^{\cdot}$) present in the solution, although they were not the dominant active species based on the experimental results described above. Ethanol and *tert*-butanol (radical scavengers for $SO_4^{\cdot -}$ and $HO^{\cdot}$, respectively) at concentrations up to 0.2 M (50 times the PDS concentration) failed to inhibit the removal of phenol (Fig. 3c) [43], suggesting $SO_4^{\cdot -}$ and $HO^{\cdot}$ present in the solution were not responsible for phenol removal. Further evidence for this conclusion was obtained from the DMPO-trapped EPR spectra. As show in Fig. 3d, although the EPR spectra of r- and n-NiO showed the typical signals of DMPO−$HO^{\cdot}$ ($a^H = a^N = 14.9$ G, marked with asterisks) and DMPOX adducts (oxidized product of DMPO, marked with circles) [27,42], their similar EPR signal intensities to those of the blank test (without catalysts) ruled out the contribution from $SO_4^{\cdot -}$ and $HO^{\cdot}$ to phenol removal (Fig. 3a, d). Radical scavenging experiments and DMPO-trapped EPR spectra further confirmed nonradical activation of PDS. Phenol removal may be related to surface activation of PDS due to the existence of $V_O$. $V_O$ with abundant localized electrons were of particular interest for the enhanced adsorption of PDS molecules. On the other hand, increased ionic strengths had negligible effects on catalytic activities (SI Fig. S13), which meant that 1) $SO_4^{\cdot -}$ was not the oxidant species responsible for phenol removal [9,44], and 2) PDS strongly interacted with NiO because $V_O$ on the NiO surface facilitated the chemical bonding with PDS molecules [9]. The surface-activated PDS-NiO complex may be the dominated reactive species responsible for phenol removal. The similar PDS activation process not relying on $SO_4^{\cdot -}$ generation also observed in CuO@PDS system [9].

To better reveal the phenol transformation pathways, the used r-NiO was subjected to quantitative solid-phase TOC analysis after freeze drying. The surface-attached TOC within 5.5 min was determined to be 13.56% (namely, 215.11 mg $L^{-1}$ phenol attached on 1.0 g·$L^{-1}$ r-NiO), very close to the corresponding theoretical TOC value associated with the removal of 217.56 mg $L^{-1}$ phenol during kinetic experiments (Fig. 3a). Besides, no degradation intermediates of phenol were detected in the reaction solution (SI Fig. S14). These results indicated that the removed phenol was predominately attached to r-NiO surface, which also explained the apparently irrational stoichiometric ratio of PDS/phenol observed in the kinetic experiments (Fig. 3b and SI Fig. S10).

To further elucidate the transformation mechanism of adsorbed phenol, a series of structural characterizations of used r-NiO was conducted. TEM images clearly showed a newly formed polymer film (Fig. 4a), which may have indicated a new oxidation polymerization mechanism for NiO@PDS Fenton-like catalysis. The resulting polymer was deliberately sandwiched between r-NiO particle agglomerates, forming a continuous film. The high-resolution TEM image showed no long-range ordered structure (SI Fig. S15) and the corresponding FFT pattern (inset in SI Fig. S15) showed dispersing diffraction rings, indicating the presence of amorphous carbon attached to the r-NiO surface [45]. Chemical mapping with SEM energy-dispersive X-ray spectroscopy also supported this conclusion, and revealed an atomically uniform distribution of C on r-NiO (Fig. 4c–f). This homogeneity could be ascribed to the homogeneous dispersion of reaction-generated polymers on the r-NiO surface. Thermogravimetric analysis further confirmed polymer formation, and the marked weight loss observed in the interval from 523 °C to 533 °C (Fig. 4b) was related to thermal decomposition of the polymer. Additionally, these results suggested that a surface-attached polymer was the main cause for gradual deactivation of the r-NiO catalyst (SI Fig. S16). The catalytic activity of spent r-NiO could be reactivated through a simple thermal treatment under an $N_2$ atmosphere (SI Fig. S16). The NiO XRD pattern after thermal reactivation evidenced the high structural stability of the r-NiO catalyst (SI Fig. S17).

The chain microstructures of the polymer deposited on the catalyst were further revealed using matrix-assisted laser desorption/ionization time-of-flight (MALDI-TOF) mass spectrometry. Fig. 5a showed the alternating structure and regioregularity of the resulting polymer, and the peaks mainly corresponded to phenol oligomers, labeled as different n-mers in parentheses, along with the detected $m/z$ values. The number-average molecular weight ($Mn$) of the polymer was determined to be 304 g·$mol^{-1}$ through gel permeation chromatography, with a narrow polydispersity index (PDI) of 1.03 (Fig. 5b). These results indicated that the resulting polymer was polymeric products of phenol, with an

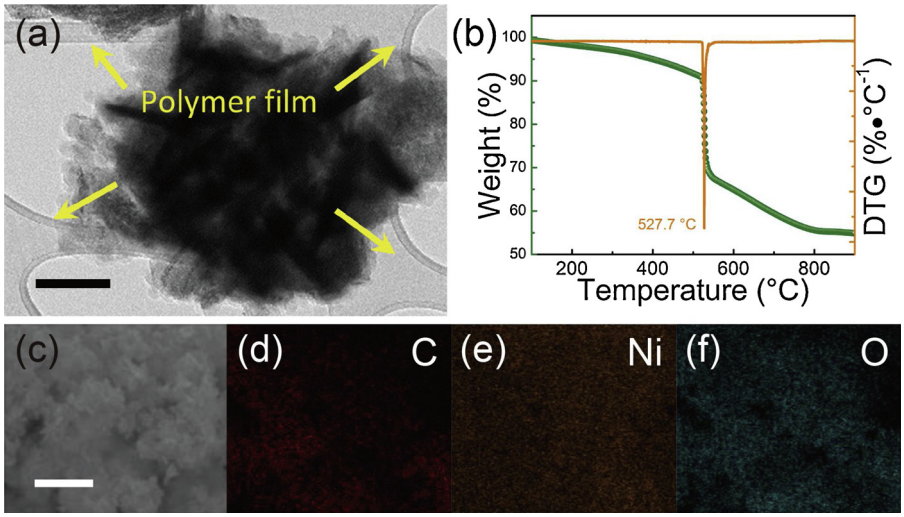


**Fig. 4.** Characterization of used catalyst. (a) TEM image. Scale bar: 200 nm. (b) Thermogravimetric analysis and derivate thermogravimetric (DTG) profiles. (c–f) SEM image and the corresponding element mappings for the C, Ni and O atoms. Scale bar: 5 μm.

alternating structure and regioregularity, low molecular weight, and narrow PDI. To further determine the formation mechanism of polymeric products, its EPR spectrum was recorded. The expected asymmetric signal of one single peak with a *g*-value of 2.0010 and linewidth of 5.8 G revealed a 34% Lorentzian and 66% Gaussian lineshape in EPR spectrum fitting (Fig. 5c). Considering that the phenoxyl radicals (SI Scheme S2) formed in aqueous solutions were short-lived intermediates, they must have reacted with each other relatively rapidly, forming various phenol oligomers through combination at the various radical sites. Therefore, the Lorentzian and Gaussian lineshapes recorded in this study corresponded to polyphenol analogue A, with electron spin–spin interactions, and polyphenol analogue B/C, with unresolved electron–nuclear hyperfine interactions, respectively (SI Scheme S3) [46–48]. Oxidation of phenol may involve one-electron transfer from phenol to surface-activated PDS-NiO complex and give the corresponding phenoxyl radical (SI Scheme S3). The deprotonated form ($C_6H_5O^-$) would be more beneficial for this oxidation reaction due to the increased reducing power of phenolate [46], which partly explained the effect of pH on the catalytic performance (SI Fig. S11). Additionally, in basic reaction medium, the coupling of free phenoxy radicals favored C—O coupling [49,50]. Based on the overall characterization and kinetic experiments, phenol removal probably followed an oxidative polymerization mechanism involved in the generation of phenoxyl radicals generated from one-electron oxidation from $C_6H_5O^-$ (the electron donor) to PDS-NiO complex (the electron acceptor) and subsequent coupling reactions. Besides, given that the powerful oxidizing capacities of $SO_4^{\cdot -}$ that may lead to the efficient elimination/mineralization of phenol, the oxidative polymerization mechanism further confirmed reactive PDS-NiO complex was the dominated reactive species due to the lower oxidation potential than $SO_4^{\cdot -}$ and $HO^{\cdot}$.

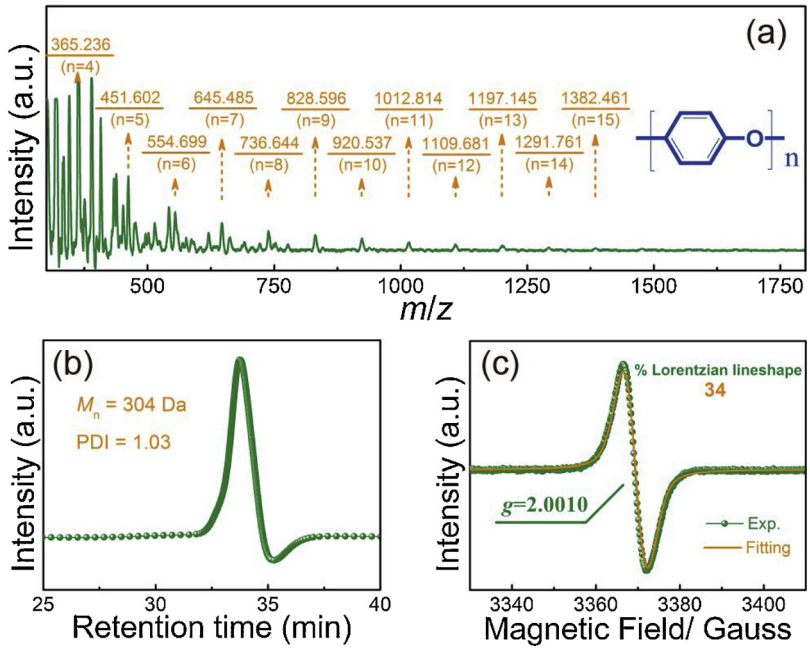


**Fig. 5.** Characterization of resulting polymeric products of phenol. (a) MALDI-TOF mass spectra. (b) Gel permeation chromatography curve and *M*n. (c) Low temperature (100 K) EPR spectra.

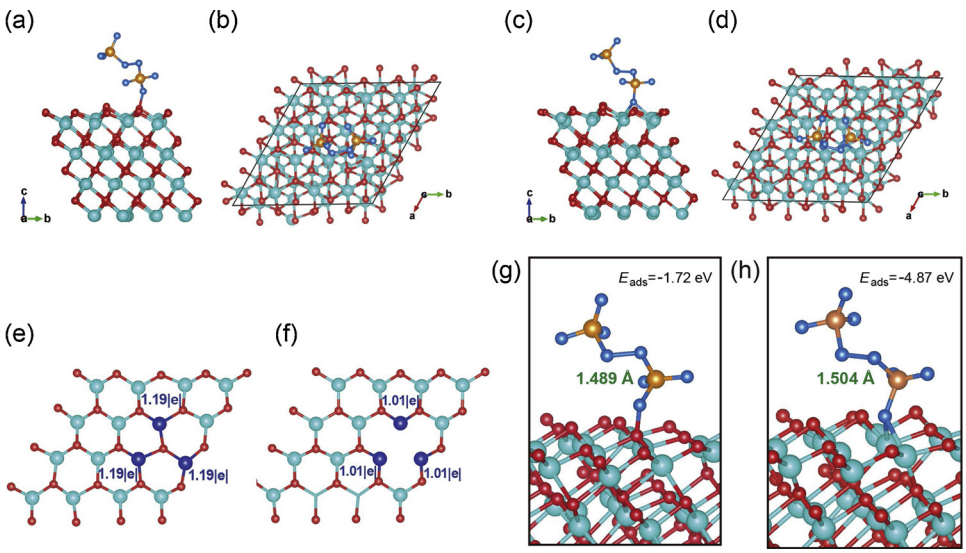


**Fig. 6.** Uncovering the mechanism of oxygen vacancy-mediated heterogeneous Fenton-like reaction. The optimized adsorption configurations: (a) Side view and (b) top view of $*S_2O_8^{2-}$ on the NiO (111) slab without $V_O$. $*S_2O_8^{2-}$ are absorbed in a monodentate mode on the NiO (111) slab without $V_O$. The O atom in $*S_2O_8^{2-}$ is adsorbed on the O atop sites in a NiO (111) slab. (c) Side view and (d) top view of $*S_2O_8^{2-}$ on the NiO (111) slab with $V_O$. The adsorption of $*S_2O_8^{2-}$ adopts a bidentate configuration, and the O atom in $*S_2O_8^{2-}$ occupy the $V_O$ and is coordinated with two neighboring Ni atoms. The blue, brown, cyan and red spheres represent O ($*S_2O_8^{2-}$), S, Ni and O (NiO) atoms, respectively. (e,f) The charge distribution on the surface of the NiO (111) slab model without and with $V_O$ after the configurations are optimized. The numbers marked in the figures represent the positive charges of metal atoms. The blue, red and cyan spheres represent Ni, O and Ni atoms, respectively. (g,h) The adsorption energies ($E_{ads}$) and O—O bond lengths of PDS molecules absorbed on the surface of NiO (111) slab model without and with $V_O$. (For interpretation of the references to colour in this figure legend, the reader is referred to the web version of this article).

### 3.4. Theoretical calculations

DFT calculations were performed to gain insight into the effect of $V_O$ on the enhanced catalytic performance using NiO (111) slabs with and without $V_O$ as models [51,52]. The optimized configurations of PDS, NiO (111) with and without $V_O$, and PDS adsorption onto NiO (111) with and without $V_O$ were calculated (Fig. 6a–d and SI Fig. S18). After generating $V_O$ on the NiO surface, the $V_O$-connected Ni atoms possessed lower positive charges of 1.01|e|, 1.01|e| and 1.02|e|, compared with 1.19|e|, 1.19|e| and 1.19|e| of the pristine NiO surface (Fig. 6e, f), indicating the electron accumulation and redistribution mediated by $V_O$. Besides, the existence of an oxygen vacancy could decrease the adsorption energy of PDS molecules (−4.87 eV) (Fig. 6g, h) and facilitate the chemical bonding with PDS molecules, implying the reactive PDS–NiO complex occurred more readily on an oxygen vacancy-rich surface. In addition, the elongated O—O bond of PDS from 1.475 Å to 1.504 Å, compared with 1.489 Å without $V_O$, was much more easily activated (Fig. 6e, f). Therefore, we can deduce that $V_O$ promoted the adsorption of PDS molecules onto the NiO surface to influence both the generation of surface-activated PDS-NiO complex and subsequent redox processes for the interaction between PDS-NiO complex and phenol, which was valuable for improving the Fenton-like catalytic performance.

According to the experimental results and theoretical calculations outlined above, an oxygen vacancy-mediated oxidative polymerization mechanism is proposed for the NiO@PDS catalytic systems (Fig. 7). First, $V_O$ in NiO successfully create more active sites, improve electron accumulation and transport, thus facilitating the bonding with PDS molecules and promoting the reactivity of PDS-NiO complex. Then, generated surface-activated PDS-NiO complex as the dominated reactive species are rapidly scavenged by phenols (mainly phenolate) to produce phenoxyl radicals through a one-electron oxidation mechanism. As a result, rapid C—O coupling of free phenoxyl radicals leads to the formation of various phenol oligomers through combination at various radical sites.

## 4. Conclusions

In conclusion, vacancy-rich NiO with extraordinary Fenton-like catalytic performance was synthesized using a facile defect engineering strategy. The $V_O$ formed through this method on the NiO surface serve as highly effective sites to facilitate the chemical bonding with PDS due to the stable adsorption configurations and efficient electron transport. Generated surface-activated PDS-NiO complex are the dominated reactive species for oxidative polymerization of phenol involved in the generation of phenoxyl radicals and subsequent coupling reactions. This study provides the detailed insights into "defect-type" catalysts for heterogeneous Fenton-like oxidative polymerization. The information acquired in this study will contribute to the development of more active "defect-type" catalysts for remediation of a wide variety of recalcitrant organics to achieve sustainable wastewater treatment for reuse of organic pollutants.

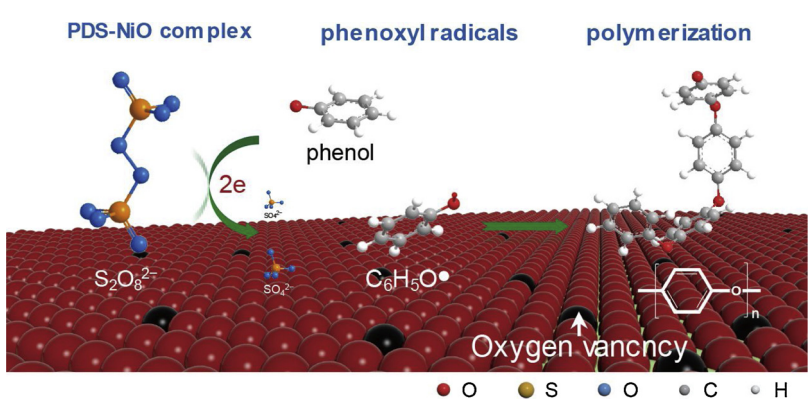


**Fig. 7.** Schematic illustration of the overall Fenton-like reaction mechanism.

## Acknowledgments

The authors appreciate the financial supports from the National Natural Science Foundation of China (No. 21676148), the Natural Science Foundation of Chongqing (No. cstc2017jcyjAX0072) and the Fundamental Research Funds for the Central Universities (No. SWU117001). We also thank Dr. Jiahui Yang (Bruker Corporation) for technical assistance of EPR spectra.

## Appendix A. Supplementary data

Supplementary material related to this article can be found, in the online version, at doi:https://doi.org/10.1016/j.apcatb.2019.04.094.

## References

[1] M.A. Shannon, P.W. Bohn, M. Elimelech, J.G. Georgiadis, B.J. Marinas, A.M. Mayes, Science and technology for water purification in the coming decades, Nature 452 (2008) 301–310.
[2] B.C. Hodges, E.L. Cates, J.H. Kim, Challenges and prospects of advanced oxidation water treatment processes using catalytic nanomaterials, Nat. Nanotechnol. 13 (2018) 642.
[3] Y. Lei, C.S. Chen, Y.J. Tu, Y.H. Huang, H. Zhang, Heterogeneous degradation of organic pollutants by persulfate activated by CuO-$Fe_3O_4$: mechanism, stability, effects of pH and bicarbonate ions, Environ. Sci. Technol. 49 (2015) 6838–6845.
[4] I.A. Ike, K.G. Linden, J.D. Orbell, M. Duke, Critical review of the science and sustainability of persulphate advanced oxidation processes, Chem. Eng. J. 338 (2018) 651–669.
[5] X.G. Duan, H.Q. Sun, Z.P. Shao, S.B. Wang, Nonradical reactions in environmental remediation processes: uncertainty and challenges, Appl. Catal. B 224 (2018) 973–982.
[6] Y.Y. Ahn, H. Bae, H.I. Kim, S.H. Kim, J.H. Kim, S.G. Lee, J. Lee, Surface-loaded metal nanoparticles for peroxymonosulfate activation: efficiency and mechanism reconnaissance, Appl. Catal. B 241 (2019) 561–569.
[7] S. Wacławek, H.V. Lutze, K. Grübel, V.V.T. Padil, M. Černík, D.D. Dionysiou, Chemistry of persulfates in water and wastewater treatment: a review, Chem. Eng. J. 330 (2017) 44–62.
[8] X.G. Duan, H.Q. Sun, S.B. Wang, Metal-Free carbocatalysis in advanced oxidation reactions, Acc. Chem. Res. 51 (2018) 678–687.
[9] T. Zhang, Y. Chen, Y.R. Wang, J. Le Roux, Y. Yang, J.-P. Croué, Efficient peroxydisulfate activation process not relying on sulfate radical generation for water pollutant degradation, Environ. Sci. Technol. 48 (2014) 5868–5875.
[10] X.G. Duan, H.Q. Sun, J. Kang, Y.X. Wang, S. Indrawirawan, S.B. Wang, Insights into heterogeneous catalysis of persulfate activation on dimensional-structured nanocarbons, ACS Catal. 5 (2015) 4629–4636.
[11] C. Kim, J.-Y. Ahn, T.Y. Kim, W.S. Shin, I. Hwang, Activation of persulfate by nanosized zero-valent iron (NZVI): mechanisms and transformation products of NZVI, Environ. Sci. Technol. 52 (2018) 3625–3633.
[12] L.W. Matzek, M.J. Tipton, A.T. Farmer, A.D. Steen, K.E. Carter, Understanding electrochemically activated persulfate and its application to ciprofloxacin abatement, Environ. Sci. Technol. 52 (2018) 5875–5883.
[13] J. Jia, C.X. Qian, Y.C. Dong, Y.F. Li, H. Wang, M. Ghoussoub, K.T. Butler, A. Walsh, G.A. Ozin, Heterogeneous catalytic hydrogenation of $CO_2$ by metal oxides: defect engineering-perfecting imperfection, Chem. Soc. Rev. 46 (2017) 4631–4644.
[14] S.B. Wang, L. Pan, J.J. Song, W.B. Mi, J.J. Zou, L. Wang, X.W. Zhang, Titanium-defected undoped anatase $TiO_2$ with *p*-type conductivity, room-temperature ferromagnetism, and remarkable photocatalytic performance, J. Am. Chem. Soc. 137 (2015) 2975–2983.
[15] Z.G. Geng, X.D. Kong, W.W. Chen, H.Y. Su, Y. Liu, F. Cai, G.X. Wang, J. Zeng, Oxygen vacancies in ZnO nanosheets enhance $CO_2$ electrochemical reduction to CO, Angew. Chem. Int. Ed. 57 (2018) 6054–6059.
[16] X.L. Xu, L. Lin, J. Huang, H. Jin, X.Z. Fang, W.M. Liu, N. Zhang, H.M. Wang, X. Wang, Engineering $Ni^{3+}$ cations in NiO lattice at atomic level by $Li^+$ doping: the roles of $Ni^{3+}$ and oxygen species for CO oxidation, ACS Catal. 8 (2018) 8033–8045.
[17] N. Zhang, A. Jalil, D.X. Wu, S.M. Chen, Y.F. Liu, C. Gao, W. Ye, Z.M. Qi, H.X. Ju, C.M. Wang, X.J. Wu, L. Song, J.F. Zhu, Y.J. Xiong, Refining defect states in $W_{18}O_{49}$ by Mo doping: a strategy for tuning $N_2$ activation towards solar-driven nitrogen fixation, J. Am. Chem. Soc. 140 (2018) 9434–9443.
[18] B.B. Zhang, L. Wang, Y.J. Zhang, Y. Ding, Y.P. Bi, Ultrathin FeOOH nanolayers with abundant oxygen vacancies on $BiVO_4$ photoanodes for efficient water oxidation, Angew. Chem. Int. Ed. 57 (2018) 2248–2252.
[19] L.J. Li, J. Zhang, J.L. Lei, J. Xu, B. Shang, L. Liu, N.B. Li, F.S. Pan, O-vacancy-enriched NiO hexagonal platelets fabricated on Ni foam as a self-supported electrode for extraordinary pseudocapacitance, J. Mater. Chem. A 6 (2018) 7099–7106.
[20] J.J. Varghese, S.H. Mushrif, Insights into the C—H bond activation on NiO surfaces: the role of nickel and oxygen vacancies and of low valent dopants on the reactivity and energetics, J. Phys. Chem. C 121 (2017) 17969–17981.
[21] D.T. Yue, C. Guo, X. Yan, R. Wang, M.Y. Fang, Y.W. Wu, X.F. Qian, Y.X. Zhao, Secondary battery inspired NiO nanosheets with rich Ni(III) defects for enhancing persulfates activation in phenolic waste water degradation, Chem. Eng. J. 360 (2019) 97–103.
[22] X.N. Li, X. Huang, S.B. Xi, S. Miao, J. Ding, W.Z. Cai, S. Liu, X.L. Yang, H.B. Yang, J.J. Gao, J.H. Wang, Y.Q. Huang, T. Zhang, B. Liu, Single cobalt atoms anchored on porous N-doped graphene with dual reaction sites for efficient Fenton-like catalysis, J. Am. Chem. Soc. 140 (2018) 12469–12475.
[23] X.B. Wang, Y.L. Qin, L.H. Zhu, H.Q. Tang, Nitrogen-doped reduced graphene oxide as a bifunctional material for removing bisphenols: synergistic effect between adsorption and catalysis, Environ. Sci. Technol. 49 (2015) 6855–6864.
[24] C.T. Guan, J. Jiang, S.Y. Pang, C.W. Luo, J. Ma, Y. Zhou, Y. Yang, Oxidation kinetics of bromophenols by nonradical activation of peroxydisulfate in the presence of carbon nanotube and formation of brominated polymeric products, Environ. Sci. Technol. 51 (2017) 10718–10728.
[25] N.A. Frigerio, An iodometric method for the macro- and microdetermination of peroxydisulfate, Anal. Chem. 35 (1963) 412–413.
[26] M.S. Wu, H.H. Hsieh, Nickel oxide/hydroxide nanoplatelets synthesized by chemical precipitation for electrochemical capacitors, Electrochim. Acta 53 (2008) 3427–3435.
[27] L.D. Liu, W.M. Wang, L. Liu, B. Yu, Y.X. Zhang, X.Q. Wu, H.W. Zhang, X. Han, Catalytic activities of dissolved and Sch-immobilized Mo in $H_2O_2$ decomposition: implications for phenol oxidation under acidic conditions, Appl. Catal. B 185 (2016) 371–377.
[28] J. Hafner, *Ab-initio* simulations of materials using VASP: density-functional theory and beyond, J. Comput. Chem. 29 (2008) 2044–2078.
[29] J.P. Perdew, J.A. Chevary, S.H. Vosko, K.A. Jackson, M.R. Pederson, D.J. Singh, C. Fiolhais, Atoms, molecules, solids, and surfaces: applications of the generalized gradient approximation for exchange and correlation, Phys. Rev. B 46 (1992) 6671–6687.
[30] C.J. Flynn, E.B.E. Oh, S.M. McCullough, R.W. Call, C.L. Donley, R. Lopez, J.F. Cahoon, Hierarchically-structured NiO nanoplatelets as mesoscale *p*-type photocathodes for dye-sensitized solar cells, J. Phys. Chem. C 118 (2014) 14177–14184.
[31] N. Behm, D. Brokaw, C. Overson, D. Peloquin, J.C. Poler, High-throughput microwave synthesis and characterization of NiO nanoplates for supercapacitor devices, J. Mater. Sci. 48 (2013) 1711–1716.
[32] J. Bao, X.D. Zhang, B. Fan, J.J. Zhang, M. Zhou, W.L. Yang, X. Hu, H. Wang, B.C. Pan, Y. Xie, Ultrathin spinel-structured nanosheets rich in oxygen deficiencies for enhanced electrocatalytic water oxidation, Angew. Chem. Int. Ed. 127 (2015) 7507–7512.
[33] Y.L. Zhu, W. Zhou, J. Yu, Y.B. Chen, M.L. Liu, Z.P. Shao, Enhancing electrocatalytic activity of perovskite oxides by tuning cation deficiency for oxygen reduction and evolution reactions, Chem. Mater. 28 (2016) 1691–1697.
[34] Q. Wang, A. Puntambekar, V. Chakrapani, Vacancy-induced semiconductor-insulator-metal transitions in nonstoichiometric nickel and tungsten oxides, Nano Lett. 16 (2016) 7067–7077.
[35] S. Park, H.S. Ahn, C.K. Lee, H. Kim, H. Jin, H.S. Lee, S. Seo, J. Yu, S. Han, Interaction and ordering of vacancy defects in NiO, Phys. Rev. B 77 (2008) 134103.
[36] A.P. Grosvenor, M.C. Biesinger, R.S.C. Smart, N.S. McIntyre, New interpretations of XPS spectra of nickel metal and oxides, Surf. Sci. 600 (2006) 1771–1779.
[37] M.C. Biesinger, B.P. Payne, L.W.M. Lau, A. Gerson, R.S.C. Smart, X-ray photoelectron spectroscopic chemical state quantification of mixed nickel metal, oxide and hydroxide systems, Surf. Interface Anal. 41 (2009) 324–332.
[38] J.W. Wan, W.X. Chen, C.Y. Jia, L.R. Zheng, J.C. Dong, X.S. Zheng, Y. Wang, W.S. Yan, C. Chen, Q. Peng, D.S. Wang, Y.D. Li, Defect effects on $TiO_2$ nanosheets: stabilizing single atomic site Au and promoting catalytic properties, Adv. Mater. 30 (2018) 1705369.
[39] J. Terhalle, P. Kaiser, M. Jütte, M. Buss, S. Yasar, R. Marks, H. Uhlmann, T.C. Schmidt, H.V. Lutze, Chlorine dioxide-pollutant transformation and formation of hypochlorous acid as a secondary oxidant, Environ. Sci. Technol. 52 (2018) 9964–9971.
[40] O.S. Furman, A.L. Teel, R.J. Watts, Mechanism of base activation of persulfate, Environ. Sci. Technol. 44 (2010) 6423–6428.
[41] M. Ahmad, A.L. Teel, R.J. Watts, Mechanism of persulfate activation by phenols, Environ. Sci. Technol. 47 (2013) 5864–5871.
[42] S.F. An, G.H. Zhang, T.W. Wang, W.N. Zhang, K.Y. Li, C.S. Song, J.T. Miller, S. Miao, J.H. Wang, X.W. Guo, High-density ultrasmall cluster and single-atom Fe sites embedded in g-$C_3N_4$ for highly efficient catalytic advanced oxidation processes, ACS Nano 12 (2018) 9441–9450.
[43] W.D. Oh, Z.L. Dong, T.T. Lim, Generation of sulfate radical through heterogeneous catalysis for organic contaminants removal: current development, challenges and prospects, Appl. Catal. B 194 (2016) 169–201.
[44] T. Zhang, H.B. Zhu, J.P. Croué, Production of sulfate radical from peroxymonosulfate induced by a magnetically separable $CuFe_2O_4$ spinel in water: efficiency, stability, and mechanism, Environ. Sci. Technol. 47 (2013) 2784–2791.
[45] Y.M. Li, Y.S. Hu, H. Li, L.Q. Chen, X.J. Huang, A superior low-cost amorphous carbon anode made from pitch and lignin for sodium-ion batteries, J. Mater. Chem. A 4 (2016) 96–104.
[46] S. Steenken, P. Neta, Transient Phenoxyl Radicals: Formaton and Properties in Aqueous Solutions, Wiley, West Sussex, England, 2003.
[47] T.N. Das, Hidden chemistry in phenoxyl radical ($C_6H_5O\cdot$) coupling reaction mechanism revealed, J. Phys. Org. Chem. 22 (2009) 872–882.
[48] L.Y. Bao, R.C. Xiong, G. Wei, Electrochemical polymerization of phenol on 304 stainless steel anodes and subsequent coating structure analysis, Water Res. 55 (2010) 4030–4038.
[49] W.A. Waters, Comments on the mechanism of one-electron oxidation of phenols: a fresh interpretation of oxidative coupling reactions of plant phenols, J. Chem. Soc. B (1971) 2026–2029.
[50] S. Kobayashi, H. Higashimura, Oxidative polymerization of phenols revisited, Prog. Polym. Sci. 28 (2003) 1015–1048.
[51] W. Zhao, M. Bajdich, S. Carey, A. Vojvodic, J.K. Nørskov, C.T. Campbell, Water dissociative adsorption on NiO(111): energetics and structure of the hydroxylated surface, ACS Catal. 6 (2016) 7377–7384.
[52] W. Zhao, A.D. Doyle, S.E. Morgan, M. Bajdich, J.K. Nørskov, C.T. Campbell, Formic acid dissociative adsorption on NiO(111): energetics and structure of adsorbed formate, J. Phys. Chem. C 121 (2017) 28001–28006.